CORTICAL OSTEON STIFFNESS: A COMPARATIVE MICROMECHANICS-BASED HOMOGENIZATION STUDY

Ilige S. Hage,[1] *Charbel Y. Seif,*[2] *& Ramsey F. Hamade*[3,*]

[1]*Department of Mechanical Engineering, Notre Dame University-Louaize, P.O. Box: 72 Zouk Mikael, Zouk Mosbeh, Lebanon*

[2]*Department of Mechanical Engineering, American University of Beirut, Riad El-Solh, Beirut 1107 2020, Lebanon*

[3]*Department of Mechanical Engineering, American University of Beirut, Riad El-Solh, Beirut 1107 2020, Lebanon*

*Address all correspondence to: Ramsey F. Hamade, Department of Mechanical Engineering, American University of Beirut, Riad El-Solh, Beirut 1107 2020, Lebanon, E-mail: rh13@aub.edu.lb

Original Manuscript Submitted: 4/10/2020; Final Draft Received: 5/10/2021

This work utilizes a novel combination of automated image segmentation and numerical homogenization solutions to provide accurate estimates of stiffness of cortical bone. Segmentation of actual cortical bone digital images (20×) provides for high-fidelity capture of lacunar-canaliculi (L-C) microstructure which, in turn, serves as geometric input to the numerical homogenization solution of osteon stiffness. Osteons are treated as lamella matrix punctuated by porous L-C inclusions namely: Haversian canals, lacunae, and canaliculi clusters. Using image segmentation, extracted geometric attributes are calculated for each individual pore within the matrix including the inclusion's area, elliptical major–minor axis length (aspect ratio), orientation, and location coordinates. Consequently, aggregate secondary osteons attributes such as area and volume fractions are calculated. Numerically, solutions of the axial Young's modulus of the cortical osteon are obtained using the established homogenization methods of Mori–Tanaka (MT) and the generalized self-consistent method (GSCM). Solutions are also obtained using the authors' own recent development dubbed the generalized stiffness formulation (GSF). To corroborate the numerical results, experimental micro-indentations hardness measurements are conducted on the same image locations in the secondary osteons. It is found that the axial Young's modulus of the cortical osteon's matrix decreases with increasing porosity (volume fraction) and aspect ratio. Although all three homogenization methods returned numerical estimates close to experimentally measured stiffness values from micro-indentation tests, the GSF stiffness results exhibit closer agreements. This is attributed to the fact that GSF, in addition to considering the inclusions' classical variables of area and shape, accounts for the geometric attributes of orientation and position of each of the actually segmented porosities in the osteon.

KEY WORDS: *cortical porosity, bone, osteon, microscale, hardness, homogenization, stiffness*

1. INTRODUCTION

Unlike cancellous (spongy) bone, cortical bone is compact and forms the outer shell of most bones. Examining a cross section of a bone taken normal to the bone's long axis (bone's transverse direction) would reveal a microscopic architecture referred to as the osteon system. Mechanically speaking, one may describe this structure as comprising lamella matrix punctuated by an array of porous inclusions of three types: Haversian canals, lacunae, and clusters of canaliculi. The presence of this assortment of micro-structural pores has a pronounced effect on the stiffness of cortical bone osteonal system.

1543–1649/21/$35.00

NOMENCLATURE

L-C	lacuna-canaliculi micro-porosity
PCNN	pulse coupled neural networks
1, 2, 3	Cartesian system longitudinal ($1 = z$) and transverse axes ($2 = x$, $3 = y$)
E_m	Young's modulus of the matrix
C_p	stiffness tensor of the pores
C_m	stiffness tensor of the matrix
C_{ha}	stiffness tensor of the Haversian inclusions
C_{la}	stiffness tensor of the lacunae inclusions
C_{ca}	stiffness tensor of the canaliculi inclusions
C^*	effective elastic stiffness tensor
P	bone porosity
E_{11}	Young's modulus along the axis of long bone (longitudinal)
E_{11}/E_m	normalized axial Young's modulus with respect to that of the matrix
S_{ijkl}	fourth-order tensor Eshelby tensor
S^I	fourth-order interior Eshelby tensor
$S^E(r)$	fourth-order exterior Eshelby tensor
RVE	representative volume
Q_{ij}	rotation tensor
R	reformulated coordinate position vector
Q_{ijkl}	transformation tensor (6×6)
i	inclusion number
$\bar{C}$	effective stiffness tensor of the composite
f_i	volume fraction of each inclusion
C_i^I	stiffness tensor of each inclusion
C^E	stiffness tensor of the matrix
A_i^E	exterior strain concentration tensor calculated for each inclusion
A_i^I	interior strain concentration tensor calculated for each inclusion
$\tilde{C}_i$	reference solid stiffness tensor
I^s	identity tensor
VF	volume fraction
AR	aspect ration
L	location
N	number of inclusions

MT	Mori–Tanaka
GSCM	generalized self-consistent method
GSF	generalized stiffness formulation
FEM	finite-element (using DEFORM) results
EXP	experimental results
NUM	numerical results using the developed homogenization code
VUL	Voigt upper limit
HSLL	Hashin–Shtrikman lower limit
G	bulk modulus
K	shear modulus
S	slope of indentation depth loading unloading curve, $S = dP/dh$
E	indenter-dependent geometry constant, $E = 0.72$
B	Vickers indenter correction factor, $B = 1.0055$
E_i	indenter modulus of elasticity, $E_i = 1141$ GPa
N_b	bone Poisson's ratio
I_{ijkl}	fourth-order identity tensor
c_I	volume fraction of the ith inclusion phase
$\bar{S}_{ijkl}$, S_{ijkl}	compliance tensors for the composite and the matrix, respectively
C^I_{klmn}	stiffness tensor for the ith inclusion phase
s_{ij}, c_{ij}	components of a compliance matrix and a stiffness matrix, respectively
A_{mnkl}	strain concentration tensor of the particulate phase relating the average strain $\bar{\varepsilon}^1_{ij}$ over a phase to the overall averaged strain $\bar{\varepsilon}_{ij}$

Greek Letters

ΔS_i^*	difference between interior and exterior Eshelby
ν_m	Poisson's ratio of the matrix
ε_d	disturbed strain
ε^*	eigenstrain
ε^0	remote strain

NOMENCLATURE *(continued)*

ν_i	indenter Poisson's ratio, $\nu_i = 0.07$	$\delta_{im}, \delta_{jn}, \delta_{in}, \delta_{jm}$	identity tensors of second order
ε^{I}_{mn}	average strain in the ith inclusion phase	σ_{ij}	components of a stress tensor
σ^{0}_{kl}	applied remote uniform stress (the superscript 0 in σ^{0}_{kl} indicates the applied remote uniform stress)	ε_{ij}	components of a strain tensor

Based on earlier work by Sun and Li (1988) for constructing effective elastic constants for 3D thick laminates, Hamed et al. (2010) introduced a hierarchical modeling approach consisting of successive homogenization steps using the Mori–Tanaka (MT) scheme, self-consistent (SC), and generalized self-consistent method (GSCM). Bone mechanical properties at the macroscale are found using results of effective elastic properties obtained at smaller scales. Also based on Sun and Li (1988), Novitskaya et al. (2013) developed a multiscale model to predict the elastic moduli of cortical and trabecular bones using SC, MT, and a homogenization scheme. Fritsch and Hellmich (2007) modeled bone at sub-micron scales for wet collagen using MT, mineralized collagen fibril using self-consistent method SC, hydroxyapatite foam using SC, and extracellular bone matrix using MT. Nikolov and Raabe (2008) estimated the elastic properties of bone at the nanoscale from the staggered arrangement of collagen molecules up to an array of parallel-mineralized fibrils using MT and Torquato and Hill's lower bound. Yoon and Cowin (2008) estimated the elastic constants of single bone osteonal lamella at different hierarchical levels. The elastic properties of human cortical bone were estimated by Barkaoui et al. (2014) by using a neural network multiscale homogenization approach. A two-level micromechanical model of cortical bone based on a generalized self-consistent method (GSCM) was developed by Neil and Guo (2006). At the first level, a single osteon was modeled as a two-phase composite having the osteonal lamellae as matrix and the Haversian canals as pores. In the second level, osteons and resorption cavities were modeled as multiple inclusions while interstitial lamellae were the matrix.

Relating to cortical bone microstructure, Hage and Hamade (2013a,b, 2014, 2015, 2016) employed magnified optical histology images of cortical bone to segment the microstructure via pulse coupled neural networks (PCNN). Particle swarm optimization (PSO) and adaptive threshold (AT) are used to optimize the PCNN networks' parameters. Consequently, unprecedented quantitative geometric data relating to each and every microscale feature within the lacuna-canaliculi (L-C) architecture of the osteon system can be collected including each pore position (porosity distribution), size, orientation, and shape (elliptical aspect ratio).

Relating to microstructure-based homogenization and in addition to the classical measures of porosity of shape and volume fraction, the authors developed expanded formulations that numerically account for a single inclusion in matrix material (Hage and Hamade, 2018). The work was further developed to account for multiple inclusions (Hage and Hamade, 2020) in matrix material based on each inclusion (pore) area, aspect ratio, orientation, and location within the matrix. Hage et al. (2018) also developed an experimentally verified closed-form expression for stiffness. These homogenization formulations were validated by contrasting numerical case solutions versus other classical homogenization schemes such as the MT scheme and generalized self-consistent method (GSCM). Stiffness findings were also corroborated via compression testing of 3D printed, porosity-containing cubes and against FEM numerical simulations.

In many "micromechanics" studies of bone, osteon porosity is typically oversimplified by considering the near-cylindrical Haversian canal as the only porosity. In this work, the authors aim to combine their recent works of high-fidelity osteon segmentation (Hage and Hamade, 2013a,b, 2014, 2015, 2016) and homogenization stiffness solution of multiple inclusions (Hage and Hamade, 2018, 2020) to relate the elastic stiffness of cortical bone to actual microscale-sized L-C features, namely lacunae, canaliculi, and Haversian canals. In the process, several (mainly secondary) osteons are segmented to reveal and quantify the geometric attributes for thousands of microsized L-C pores. Segmentations of the magnified images reveal geometric characteristics of individual microscopic pores including each pore area, aspect ratio, orientation, and location coordinates.

To determine the cortical bone stiffness as function of the porous microarchitecture, this work applies the generalized stiffness formulation (GSF) homogenization method that returns micromechanics-based calculations of stiffness that employs the quantified geometric attributes of all identified pores within the osteon. The resulting stiffness values from the GSF method are reported alongside those obtained using the established method of the GSCM and that of MT. Experimental microindentation tests were used to gauge the accuracy of numerical estimates of stiffness values for these three homogenization methods. The steps taken in this work are summarized as follows:

- Secondary osteons are treated as multiphase composite having the osteonal lamellae as matrix with multiple porosities: Haversian canals, lacunae, and canaliculi clusters.
- Utilizing magnified, high-fidelity histology slides of cortical-porosity-containing osteons and employing PCNN for segmentation, determine basic geometric attributes (namely individual size, shape, orientation, and location coordinates) of cortical L-C cortical porosity.
- In order to calculate the respective Eshelby tensors for each porous inclusion, derived geometric measures of cortical porosity for the total secondary osteon had to be determined including aspect ratios (shapes) and volume fractions (sizes) for all of the three types of pores. The aspect ratio measure was determined for each pore in order to classify each inclusion's shape into cylindrical, elliptical, or irregular.
- Said measures are used as input for microbased homogenization scheme. From the homogenization method, an equivalent modulus of elasticity specific for the cortical bone sample relating the axial Young's modulus (E_{11}) to L-C lumped values of pores' area, circular radius, and elliptical major–minor axis lengths (aspect ratio vectors), orientations, and the location coordinates for each individual pore within the matrix.
- Experimental microindentation hardness tests on same osteons spots of interest are employed. Axial Young's modulus values are calculated from slopes of unloading curves (Section 4).
- Calculated experimental stiffness values are compared for all three homogenization methods and against indentation-derived stiffness values (Section 5).

2. HOMOGENIZATION METHODS IMPLEMENTATION

This work aims to determine the effective Young's modulus of secondary osteon where the osteonal lamellae are treated as matrix while the Haversian canals, lacunae, and canaliculi clusters as porosities. To determine the effective stiffness tensor of cortical bone as function of the porous microarchitecture, this work applies the GSF homogenization method that returns numerical micro-mechanics-based calculations of stiffness as function of the quantified geometric attributes of all identified pores within the osteon. The same formulation was applied by the authors in Hage and Hamade (2017) where GSF was applied to determine bone ring stiffness modulus under compression along the longitudinal and transverse directions at the macroscale starting from the image segmentation procedure at the microscale. In Hage and Hamade (2017), micro-porosities, lacunae, canaliculi and Haversian canals were segregated and analyzed geometrically to provide the inputs for GSF. Performed were analytical stiffness calculations of a ring bone at different spots along a radial line at the macroscale. The results were verified against experimental indentation tests at each spot (at each radius). In addition, the transverse stiffness was verified against compression experimental testing and FEM simulation of similar tests. The resulting stiffness values from the GSF method were reported alongside the results of two other established homogenization methods: the GSCM and that of MT.

2.1 GSCM

To produce statistical homogeneity field in the composite, the generalized self-consistent method (Neil and Guo, 2006) applies independent uniform stress boundary conditions to produce homogeneous fields in a homogeneous body. Energy equivalence postulates (Budiansky, 1965) that strain energy of the composite is equal to the sum of strain energy for all components:

$$\bar{S}_{ijkl}\sigma^0_{ij}\sigma^0_{kl} = S_{ijkl}\sigma^0_{ij}\sigma^0_{kl} + \sum_{i=1}^{N-1} c_I \left[\frac{1}{2}(\delta_{im}\delta_{jn} + \delta_{in}\delta_{jm}) - S_{ijkl}C^I_{klmn}\right]\sigma^0_{ij}\varepsilon^I_{mn} \tag{1}$$

where ε^I_{mn} is the average strain in the Ith inclusion phase, c_I is the volume fraction of the Ith inclusion phase, σ^0_{kl} is applied remote uniform stress, $\bar{S}_{ijkl}$ and S_{ijkl} are compliance tensors for the composite and the matrix, respectively, C^I_{klmn} is the stiffness tensor for the Ith inclusion phase. The subscript 0 in σ^0_{ij} and σ^0_{kl} indicates the applied remote uniform stress: δ_{im}, δ_{jn}, δ_{in}, and δ_{jm} that are identity tensors of second order (Neil and Guo, 2006).

The elastic constants of the composite can be estimated by decomposing the general energy equivalence according to the five independent uniform stress boundary conditions (Neil and Guo, 2006): 1 – plane-strain biaxial tension $\sigma^0_{11} = \sigma^0_{22} = \sigma_0$, $\varepsilon^0_{33} = 0$, 2 – in-plane biaxial tension compression $\sigma^0_{11} = \sigma_0$, $\sigma^0_{22} = -\sigma_0$, 3 – out-of-plane shear ($\sigma^0_{13} = \sigma^0_{31} = \sigma_0$), 4 – uniaxial tension $\sigma^0_{33} = \sigma_0$, 5 – hydrostatic tension $\sigma^0_{11} = \sigma^0_{22} = \sigma^0_{33} = \sigma_0$. Resolving the five equations to determine the five unknown effective elastic constants of the composite, and to evaluate the components of the average strain ε^{II}_{11}, ε^{II}_{22}, ε^{II}_{33} for each individual inclusion is necessary [see Neil and Guo (2006) for detailed treatment of boundary conditions]. A system of nonlinear algebraic equations needs to be solved using the Newton–Raphson numerical method in order to determine the secondary osteon's effective elastic stiffness tensor, C^*.

In this work, the GSCM methodology is implemented using input parameters (namely volume fraction and aspect ratio) obtained from the porosity output from segmented images employing the PCNN–PSO-AT methodology previously developed by the authors Hage and Hamade (2013a,b, 2014, 2015, 2016). For coding the method, the steps are outlined by the flowchart in Fig. 1 where the desired output (C^*) designates the stiffness tensor of the homogenized secondary osteon. In order to calculate the stiffness tensor of the matrix C_m and the inclusions C_{ha}, C_{la}, C_{ca} (ha for the Haversian, la for the lacunae, and ca for the canaliculi), Eqs. (2) and (3) are used to calculate the shear, G, and bulk, K, moduli

$$G = \frac{E}{2*(1+\nu)} \tag{2}$$

$$K = \frac{E}{3*(1-2*\nu)} \tag{3}$$

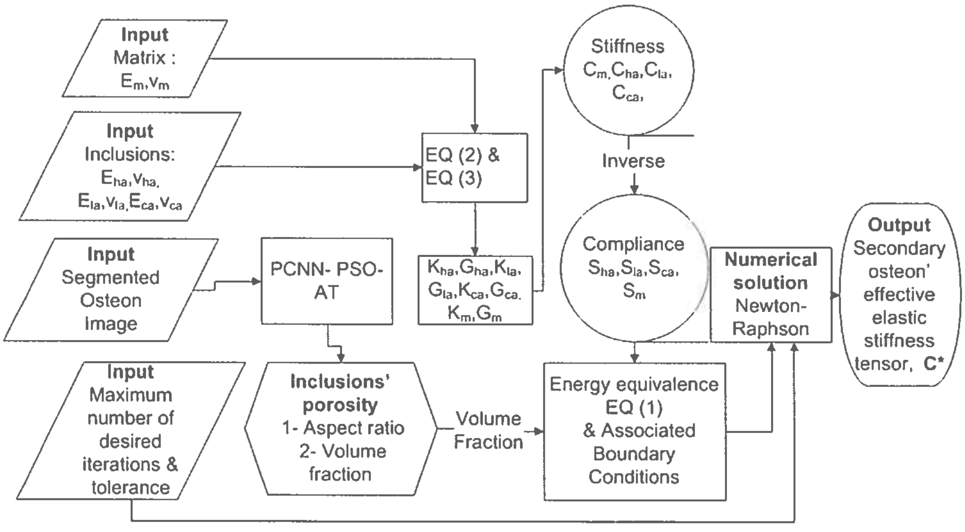

FIG. 1: GSCM implementation with PCNN-PSO-AT applied to cortical bone secondary osteons

The compliance matrices for the Haversian (ha), lacunae (la), and canaliculi (ca) are S_{ha}, S_{la}, S_{ca}, respectively. The effective elastic constants of a composite can be estimated by decomposing the general energy equivalence Eq. (1) found by solving Eq. (1) and the five boundary conditions equations (Fritsch and Hellmich, 2007) applied and solved numerically using the Newton–Raphson method in order to determine C^*.

2.2 MT

In order to calculate the effective properties of composites, the MT method by Mori and Tanaka (1973) approximates the average stress field based on the equivalent classical work of Eshelby (1957, 1961). The MT methodology is implemented using input parameters (volume fraction and aspect ratio) obtained from the segmented images using the scheme described in the flowchart schematic of Fig. 2. In a fashion similar to that for GSCM and in order to calculate the stiffness tensor of the matrix C_m and the inclusions C_{ha}, C_{la}, C_{ca}, Eqs. (2) and (3) are used to calculate the shear, G, and bulk, K, moduli. Eshelby tensor is calculated for each individual inclusion shape. By taking volume averages, the expression for the effective elastic tensor of a two-phase particulate composite (volume fraction, φ, of particulate phase) can be written by Parnell and Grimal (2012) as

$$C^*_{ijkl} = C^0_{ijkl} + \varphi \left(C^1_{ijmn} - C^0_{ijmn}\right) A_{mnkl} \tag{4}$$

where C^0_{ijkl} and C^1_{ijkl} are stiffness tensor of the inclusion and matrix, respectively, and A_{mnkl} is the strain concentration tensor of the particulate phase (phase 1). The average strain $\bar{\varepsilon}^1_{ij}$ over this phase is related to the overall averaged strain $\bar{\varepsilon}_{ij}$ by

$$\bar{\varepsilon}^1_{ij} = A_{ijkl}\bar{\varepsilon}_{kl} \tag{5}$$

A secondary concentration tensor, B_{ijkl} is defined to relate the averaged strain over the particulate phase to that of the matrix phase $\bar{\varepsilon}^1_{ij}$ via

$$\bar{\varepsilon}^1_{ij} = B_{ijkl}\bar{\varepsilon}^0_{kl} \tag{6}$$

Substituting Eq. (6) in the standard equation for total averaged strain yields

$$\bar{\varepsilon}_{ij} = \varphi\bar{\varepsilon}^1_{ij} + (1-\varphi)\bar{\varepsilon}^0_{ij} = \left[\varphi B_{ijkl} + (1-\varphi)\delta_{ik}\delta_{jl}\right]\bar{\varepsilon}^0_{kl} \tag{7}$$

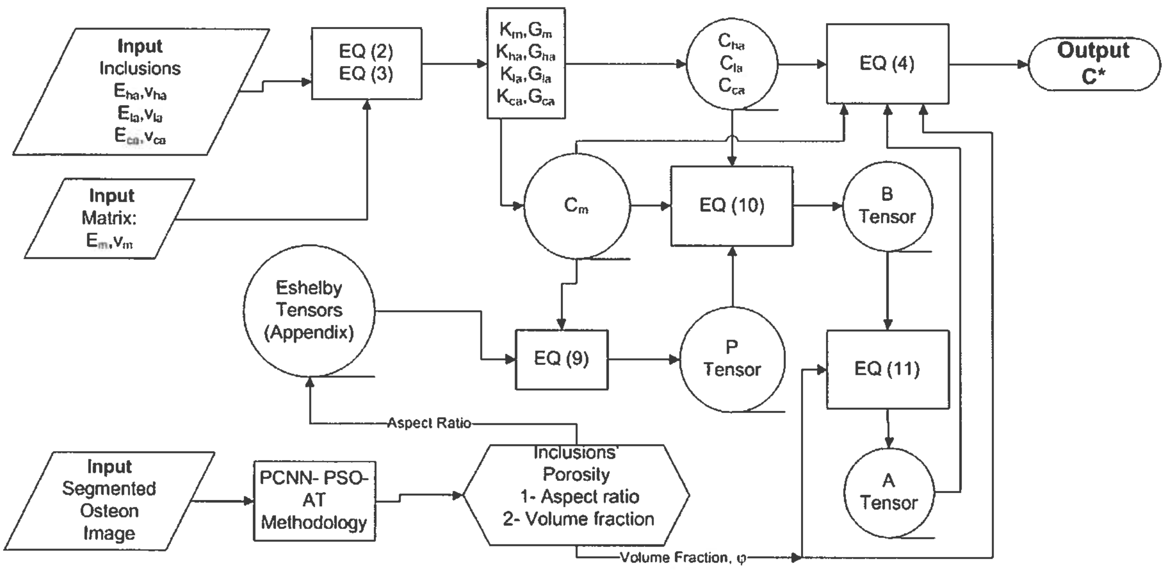

FIG. 2: MT implementation with PCNN-PSO-AT applied to cortical bone secondary osteons

Also substituting in Eq. (5) gives

$$\bar{\varepsilon}^{1}_{ij} = A_{ijkl}\left[\varphi B_{klpq} + (1-\varphi)\delta_{kp}\delta_{lq}\right]\bar{\varepsilon}^{0}_{pq} \tag{8}$$

where P_{mnkl} is defined via the classical Eshelby tensor (Eshelby, 1957, 1961)

$$S_{ijkl} = C^{0}_{ijmn}P_{mnkl} \tag{9}$$

A consistent choice for B_{ijkl} that is valid near $\varphi = 0$ and $\varphi = 1$ is to choose $B_{ijkl} = A^{\mathrm{dil}}_{ijkl}$ where the superscript dil denotes the "dilute strain concentration tensor" (Parnell et al., 2012)

$$B_{ijmn}\bar{B}_{mnkl} = I_{ijkl};\quad \bar{B}_{mnkl} = I_{ijkl} + P_{ijmn}\left(C^{1}_{mnkl} - C^{0}_{mnkl}\right) \tag{10}$$

where I_{ijkl} is the fourth-order identity tensor.

For consistency with Eq. (4), the following relation should hold:

$$B_{ijpq} = A_{ijkl}\left[\varphi B_{klpq} + (1-\varphi)\delta_{kp}\delta_{lq}\right] \tag{11}$$

The stiffness tensor of the homogenized secondary osteon (C^{*}) is finally returned using Eq. (4).

2.3 GSF Scheme

Hage and Hamade (2020) extended the traditional homogenization formulations for finite volume to allow for the consideration of multiple inclusions and their spatial distributions along with their corresponding individual geometric attributes. For all inclusions present in different states, a combined homogenization formulation (dubbed GSF) is posed for summing five geometric attributes: volume fraction (VF), shape or aspect ratio (AR, which is accounted for via the Eshelby tensor expression), 3D orientation (θ, φ, γ), location (position within the domain) within the matrix (r), and number of inclusions in the domain. This work was based partly on the superposition of strain field principle described by Li et al. (2007) for one inclusion in finite and infinite domains (without considering the effect of location). The result was a combined formulation for the effective stiffness tensor of a finite domain that accounts for the combined effects of multiple inclusions attributes.

In Hage and Hamade (2020), an illustration of a representative volume composite Ω_u (and its global coordinate system) containing multiellipsoid inclusions Ω^{i}_{I} (with their local coordinate systems) of various orientations. Also shown is each inclusion's corresponding coordinate system used to locate it. In the RVE, the composite universe with its multiple inclusions is utilized to determine the location of each inclusion. More details of the calculation of all variables are found in Hage and Hamade (2020). One ellipsoidal inclusion is represented in Hage and Hamade (2018). The schematic is a representation of an ellipsoidal-shaped inclusion with its 3D orientation (θ, φ, γ), minor and major axis, and assigned location with respect to the global coordinate system (Hage and Hamade, 2020). The major and minor axes were used to calculate the AR and allow the inclusion to be classified based on the above-described shapes. To calculate the matrix's effective stiffness tensor (C_m), the Young's modulus and Poisson's ratio (E_m, ν_m) for the matrix were assigned as obtained from literature. For the pores' stiffness tensor (C_p), pores were assigned null properties: ($E_p = 0$ GPa, $\nu_p = 0$). The effective elastic stiffness tensors (C^{*}) of secondary osteons were obtained, from which axial Young's modulus was obtained as function of volume fraction using above-mentioned methods. The "effective" elastic stiffness tensors (C^{*}) of cortical secondary osteons were obtained. Utilizing these tensors, axial Young's modulus values were obtained as a function of volume fraction of each pore type as well as individual geometric shape attributes (aspect ratio). To calculate the matrix's isotropic stiffness tensor, C_m, the Young's modulus and Poisson's ratio (E_m, ν_m) for the matrix were assigned as obtained from literature (for the osteonal lamellae matrix the assigned Young's modulus is $E = 20.8$ GPa (Rho et al., 1999) and Poisson's ratio $= 0.24$ (Budyn and Hoc, 2010). This GSF is suited for aggregating the geometric attributes of all inclusions. A large digital output of segmented cortical porosity images from the PCNN-PSO-AT methodology (Hage and Hamade, 2013a,b, 2014, 2015, 2016) served as the input to the GSF calculations in this work.

The numerical solution scheme is described in Fig. 3 and is summarized below. The desired output is C^*, which designates the stiffness tensor of the homogenized secondary osteon. In a fashion similar to that for GSCM and in order to calculate the stiffness tensor of the matrix C_m and the inclusions C_{ha}, C_{la}, C_{ca}, Eqs. (2) and (3) are used to calculate the shear (G) and bulk (K) moduli. Interior and exterior Eshelby tensors are calculated for each inclusion's shape and type. Equation (12) calculates the rotation transformation tensor.

$$Q_{ijkl} = \begin{pmatrix} Q_{11}^2 & Q_{21}^2 & Q_{31}^2 & \sqrt{2}Q_{11}Q_{21} & \sqrt{2}Q_{21}Q_{31} & \sqrt{2}Q_{11}Q_{31} \\ Q_{12}^2 & Q_{22}^2 & Q_{32}^2 & \sqrt{2}Q_{11}Q_{22} & \sqrt{2}Q_{22}Q_{32} & \sqrt{2}Q_{12}Q_{32} \\ Q_{13}^2 & Q_{23}^2 & Q_{33}^2 & \sqrt{2}Q_{13}Q_{23} & \sqrt{2}Q_{23}Q_{33} & \sqrt{2}Q_{13}Q_{33} \\ \sqrt{2}Q_{11}Q_{12} & \sqrt{2}Q_{21}Q_{22} & \sqrt{2}Q_{31}Q_{32} & Q_{11}Q_{22}+Q_{21}Q_{12} & Q_{21}Q_{32}+Q_{31}Q_{22} & Q_{11}Q_{32}+Q_{31}Q_{12} \\ \sqrt{2}Q_{12}Q_{13} & \sqrt{2}Q_{22}Q_{23} & \sqrt{2}Q_{32}Q_{33} & Q_{12}Q_{23}+Q_{22}Q_{13} & Q_{22}Q_{33}+Q_{32}Q_{23} & Q_{12}Q_{33}+Q_{32}Q_{13} \\ \sqrt{2}Q_{11}Q_{13} & \sqrt{2}Q_{21}Q_{23} & \sqrt{2}Q_{31}Q_{33} & Q_{11}Q_{23}+Q_{21}Q_{13} & Q_{21}Q_{33}+Q_{31}Q_{23} & Q_{11}Q_{33}+Q_{31}Q_{13} \end{pmatrix} \tag{12}$$

where Q terms are function of the transformation matrix

$$Q_{ij} = R_x1(\theta) * R_x2(\varphi) * R_x3(\gamma) = \begin{bmatrix} 1 & 0 & 0 \\ 0 & \cos\theta & -\sin\theta \\ 0 & \sin\theta & \cos\theta \end{bmatrix} * \begin{bmatrix} \cos\varphi & 0 & \sin\varphi \\ 0 & 1 & 0 \\ -\sin\varphi & 0 & \cos\varphi \end{bmatrix} * \begin{bmatrix} \cos\gamma & -\sin\gamma & 0 \\ \sin\gamma & \cos\gamma & 0 \\ 0 & 0 & 1 \end{bmatrix}$$

$$\begin{bmatrix} x_1 \\ x_2 \\ x_3 \end{bmatrix} = Q_{ij} \begin{bmatrix} x_1' \\ x_2' \\ x_3' \end{bmatrix}$$

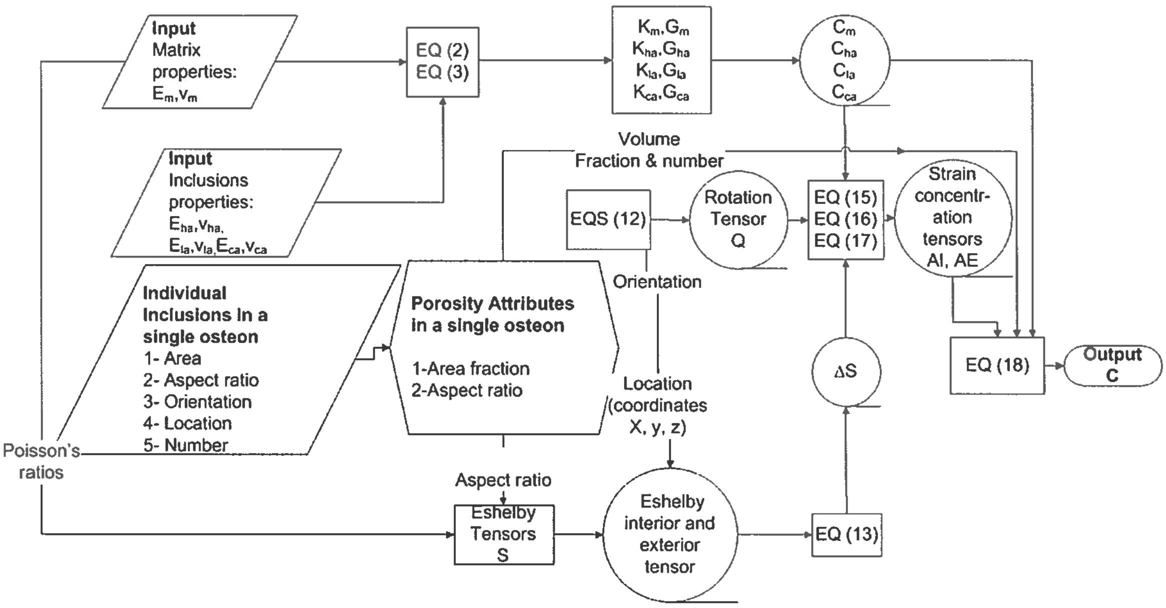

FIG. 3: GSF homogenization implementation with PCNN-PSO-AT methodology applied to cortical bone secondary osteons

Equations (13) and (14) calculate the overall averaged Eshelby over the whole universe (interior–exterior) for each inclusion is based on the location of the inclusion.

$$\Delta S_i^* = \langle S_i^{I,*}(\tilde{C}_i, f = f_i)\rangle_{\Omega_E} - \langle S_i^{E,*}(\tilde{C}_i, f = f_i)\rangle_{\Omega_I} \tag{13}$$

$$\langle \ldots \rangle_{\Omega_u} = \frac{1}{|\Omega_u|} \int\limits_{\Omega_u} \ldots d\Omega_u \tag{14}$$

Equations (15)–(17) give the interior and exterior strain concentration tensors for each inclusion.

$$A_i^E = I^s - \tilde{C}_i^{-1} : (\tilde{C}_i - C^E) : \Delta S_i^* \tag{15}$$

$$A_i^I = I^s - \tilde{C}_i^{-1} : (\tilde{C}_i - C_i^I) : \Delta S_i^* \tag{16}$$

$$\tilde{C}_i = aC_i^I + (1-a)C^E, \quad 0 \leq a \leq 1 \tag{17}$$

Equation (18) returns the effective stiffness tensor of the composite for multiple inclusions.

$$\begin{aligned} \bar{C} = &\left[\sum_{i=1}^{N} f_i * C_i^I : Q_{ijkl} : A_i^E + \left(1 - \sum_{i=1}^{N} f_i\right) \sum_{i=1}^{N} C^E : Q_{ijkl} : A_i^I\right] \\ &: \left[\sum_{i=1}^{N} f_i * Q_{ijkl} : A_i^E + \left(1 - \sum_{i=1}^{N} f_i\right) \sum_{i=1}^{N} Q_{ijkl} : A_i^I\right]^{-1} \end{aligned} \tag{18}$$

3. SEGMENTATION OF MICROPOROSITY

Presented in this section are representative segmentation results extracted using the PCNN-PSN-AT methodology (Hage and Hamade, 2013a,b, 2014, 2015, 2016). Employing digital image segmentation via MATLAB®, porosity (Haversian canals, lacunae, and canaliculi) in secondary osteons is segregated into separate segments, each containing the relevant porosity. First, the automatic detection of cortical bones Haversian osteonal boundaries (cement lines) is performed per Hage and Hamade (2015). Then, the features located inside the cement lines were extracted as described in Hage and Hamade (2013a,b, 2014, 2015, 2016).

Of the numerous bone image slides segmented and analyzed in this work, Figs. 4–6 show three typical segmented examples (dubbed bone samples 1, 2, and 3). Each one of these figures is an original image captured at 20× magnification showing the L-C inclusions. Each figure contains an original image lying in the transverse (2,3) plane. Also shown are segmented (b) secondary osteon with demarcated cement line, (c) Haversian canal, (d) canaliculi clusters, and (e) lacunae inclusions. For each of these three L-C inclusions, the volume fraction values are listed. Also listed is the total volume fraction (VF) value or the sum of the three values for the Haversian canal, canaliculi clusters, and lacunae inclusions. For bone sample 1 in Fig. 4, the volume fraction of the Haversian, canaliculi clusters, and lacunae inclusions was found to be 6.7%, 12%, and 0.99%, respectively, of the total area of the secondary osteon. Adding, the total volume fraction of the secondary osteon porosity was found to be 19.69%. For bone sample 2 in Fig. 5, the volume fraction of the Haversian, canaliculi clusters, and lacunae inclusions was found to be 6.1%, 21.5%, and 1.1%, respectively, of the total area of the secondary osteon. Adding, the total volume fraction of the secondary osteon porosity was found to be 28.7%. For bone sample 3 in Fig. 6, the volume fraction of the Haversian, canaliculi clusters, and lacunae inclusions was found to be 8.2%, 26.7%, and 1.9%, respectively, of the total area of the secondary osteon. Adding, the total volume fraction of the secondary osteon porosity was found to be 36.8%.

This segmentation method was verified by Hage and Hamade (2013a) to be very accurate in segregating and demarcating micron-sized entities in images of L-C inclusions of cortical bones. See for example Table 1 in Hage and Hamade (2013a), which lists impressive statistical metrics for evaluating the quality of resulting inclusion segments using PCNN-PSO-AT methodology. To prove the quality of the resultant segmented images, the table lists the values of the metrics [precision, recall, sensitivity, specificity, accuracy, and f-index (or dice) indices] of the segmented

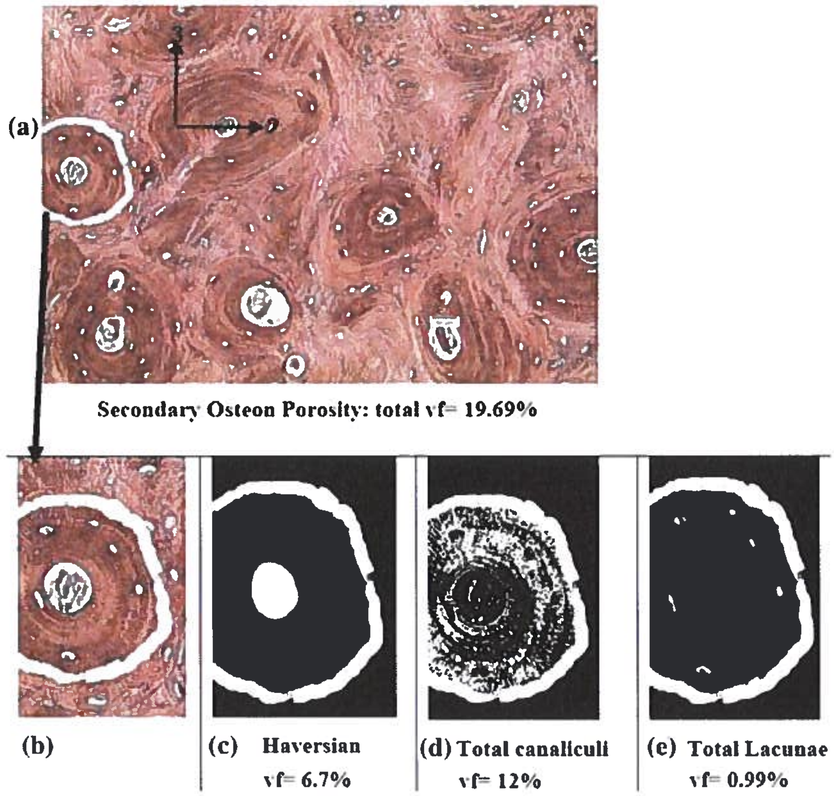

FIG. 4: Bone sample 1 L-C inclusions. Shown are (a) original image (20× magnification) lying in the transverse (2, 3) plane. Also shown are segmented (b) secondary osteon with demarcated cement line, (c) Haversian canal, (d) canaliculi clusters, and (e) lacunae inclusions along with their volume fractions.

images. Precision is described as percentage of the accurately identified regions, sensitivity is rate of the object of interest that is perfectly detected, specificity quantifies the capability of not detecting the unwanted regions, accuracy is related to the rate of correct results, and dice reflects how much the segmented images reflect the true segmented regions of interest.

Areas, circular radius, and elliptical major–minor axis length, orientations, the coordinates in the transverse direction for each one of the porosities (individually) in the images shown in Fig. 4 are calculated. These values are used to calculate derived measures such as volume fraction vectors, orientations, and location coordinates in the matrix as well as the aspect ratio vectors which represents the input vector to extract the Eshelby tensors using the closed-form equations as per Mura (1987). The images allow the determination of the input vector parameters in the long bone's transverse direction (2, 3) as marked in Fig. 4(a). As for the long bone's axial direction 1 (depth), the inputs are estimated based on the following classifications of inclusions into these categories:

- The lacunae were grouped into three categories (depending on the axis length determined using image segmentation):
  - Spherical inclusions with radius $a1 = a2 = a3$
  - Prolate spheroid inclusions $a3 > a2 = a1$
  - Oblate spheroid $a3 < a2 = a1$
- The canaliculi were grouped into two categories:

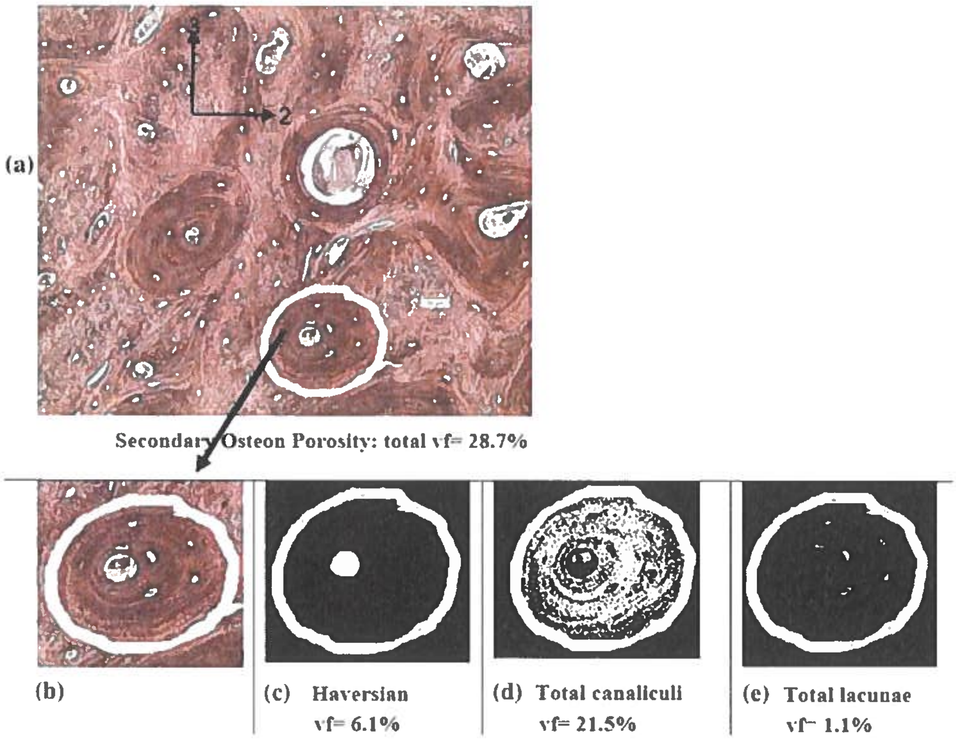

FIG. 5: Bone sample 2 L-C inclusions. Shown are (a) original image (20× magnification) lying in the transverse (2,3) plane. Also shown are segmented (b) secondary osteon with demarcated cement line, (c) Haversian canal, (d) canaliculi clusters, and (e) lacunae inclusions along with their volume fractions.

   - Prolate spheroid $a3 > a2 = a1$
   - Oblate spheroid $a3 < a2 = a1$

- The Haversian canals were grouped into two categories:
   - Circular cylinder $a1 \rightarrow \infty$
   - Elliptical cylinder $a1 \rightarrow \infty$

Microporosity segmentation gives rise to volume fraction calculations based on depth estimates from the shape configurations explained above. For each pore type, volume of each pore is calculated from the segmented image area multiplied by its axial depth. Repeating for each pore, the aggregate volume fraction is calculated.

4. MICROINDENTATION MEASUREMENTS

To conduct microindentation experiments on osteons, sectioned bone specimens of 2 mm thick were cut from mid-diaphysis section of long femur bovine bone collected fresh from a butcher. A light microscope (attached to the indenter setup Nexus 4304) equipped with a digital camera [Olympus SC30 digital microscope camera, based on a 3.3-megapixel charged-coupled device (CCD) chip with a complementary metal–oxide–semiconductor (CMOS) color sensor] was used for digital imaging. The test surfaces were lightly polished according to the following procedure:

- The bones were ground with silicon carbide (SiC) abrasive papers of progressively finer grit sizes (600, 800, and 1200 grit).

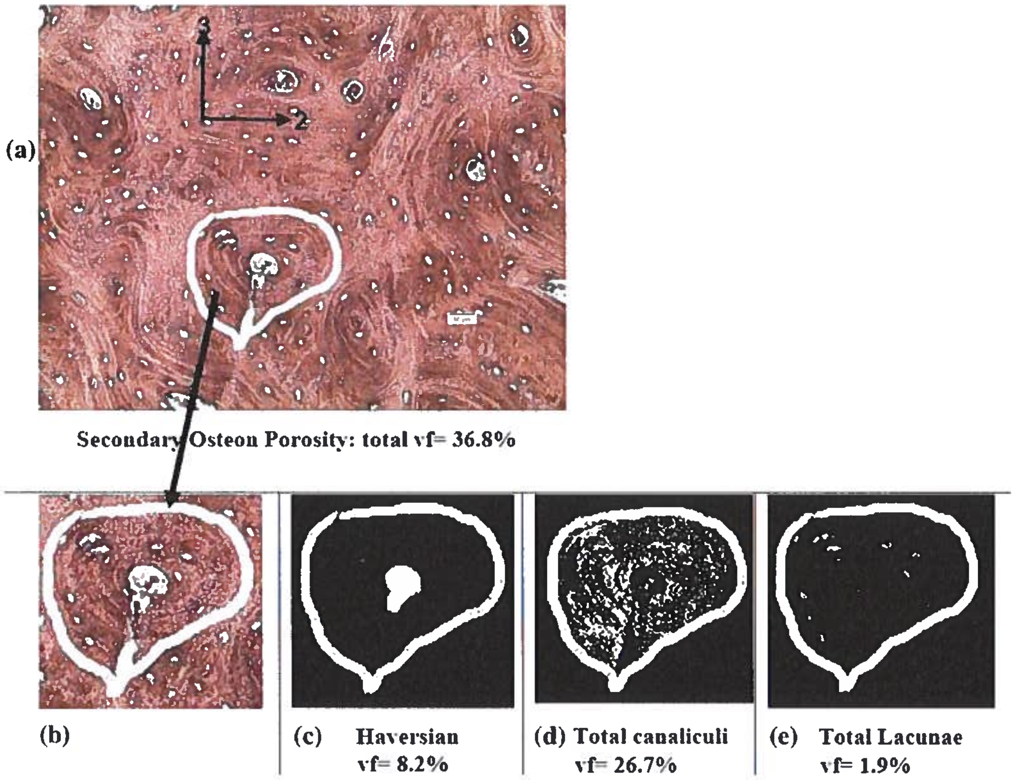

FIG. 6: Bone sample 3 L-C inclusions. Shown are (a) original image (20× magnification) lying in the transverse (2,3) plane. Also shown are segmented (b) secondary osteon with demarcated cement line, (c) Haversian canal, (d) canaliculi clusters, and (e) lacunae inclusions along with their volume fractions.

TABLE 1: Metrics for evaluating the quality of resulting inclusion segments using PCNN-PSO-AT methodology

		Bone sample 1			
Metric	Precision rate	Sensitivity	Specificity	Accuracy	Dice
Haversian	0.99	0.83	0.98	0.99	0.84
Lacunae	0.84	0.87	0.95	0.99	0.86
Canaliculi	0.92	0.96	0.96	0.92	0.87
		Bone sample 2			
Metric	Precision rate	Sensitivity	Specificity	Accuracy	Dice
Haversian	0.99	0.83	0.99	0.99	0.90
Lacunae	0.85	0.91	0.99	0.99	0.88
Canaliculi	0.95	0.88	0.96	0.82	0.87
		Bone sample 3			
Metric	Precision rate	Sensitivity	Specificity	Accuracy	Dice
Haversian	0.97	0.75	0.99	0.99	0.85
Lacunae	0.83	0.94	0.99	0.99	0.88
Canaliculi	0.89	0.96	0.86	0.83	0.86

The sectioned specimens were wet-polished on a rotary wheel at constant speed with 2400 grit SiC papers. Additional polishing was done on a nap-less cloth. After polishing, surface roughness was less than 30 nm.

Microindentation experiments in accordance with ASTM E384-11e1 Standard (test method for Vickers hardness of materials) were performed on the bone slices prepared. Bone slices were analyzed using the optical microscope equipped with the microindenter Nexus 4304 and the osteons at the same location and orientation similar to those digitally imaged are indented at a (very small) load of 20 gf and dwelling time of 15 s. Figure 7 shows the performed indentions on 19 osteons that were imaged using the BX 41 M LED microscope at 10× magnification.

The osteonal axial Young's modulus was calculated using force-depth data generated by the Vickers hardness tests. The axial Young's moduli of these osteons were determined experimentally, using force vs. depth data extracted from microindentation tests. Figure 8 shows such a force vs. depth plot of an indent performed on one osteon. Using force-depth data for each osteon, and the Oliver and Pharr method (Oliver and Pharr, 2010), the unloading fitted using a power-law relation to determine $S = dP/dh$ suggested the area of the indents were calculated using the scale bar (100 micrometer). Finally, Young's modulus value of each osteon was determined. According to Oliver and Pharr (2010), calculating the axial Young's modulus for one osteon requires the input values for the diamond Vickers indenter: $\varepsilon = 0.72$, $\beta = 1.0055$, $E = 1141$ GPa, $\nu = 0.07$.

5. OSTEON STIFFNESS: MICROSCALE HOMOGENIZATION RESULTS

Porosity output from segmentation work (Section 3) returned quantified porosity for several osteons. For these osteons and as per Section 2, values for the normalized axial stiffness tensor, and consequently Young's modulus normalized with respect to that of the matrix, E_{11}/E_m, were determined according to: (1) Mori–Tanaka (MT), (2) generalized self-consistent method (GSCM), and (3) developed homogenization code (GSF). The lacunae, canaliculi, and Haversian canals were treated as voids (Young's modulus $E = 0$ GPa and Poisson's ratio $= 0$). The assigned properties

FIG. 7: Microindentation marks on the osteon surface due to the performed Vickers tests

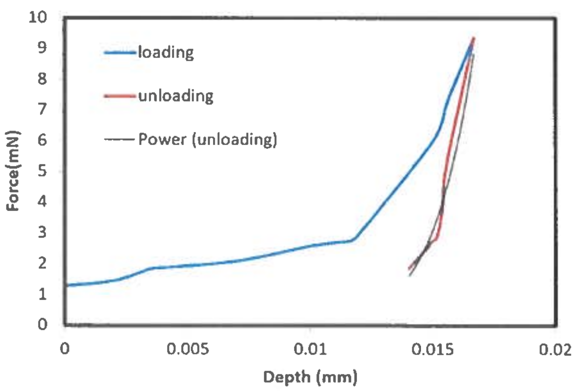

FIG. 8: Microindentation experimental force vs. depth data performed on osteon

for the osteonal lamellae matrix are Young's modulus E = 20.8 GPa (Rho et al., 1999) and Poisson's ratio = 0.24 (Budyn and Hoc, 2010).

Osteons having aggregate inclusions' aspect ratios of 0.5775, 0.5865, and 0.6070 are grouped and segregated into their corresponding volume fractions. In addition to the experimental results from the microhardness tests, the normalized axial Young's modulus values are reported for each osteon employing the three different homogenization methods alluded to above. As it was verified in Hage and Hamade (2020), GSF uses as input independent orientations and aspect ratios of each inclusion since the tensor formulation takes into account individual inclusion variables as tensor to be input. However, for the case of osteonal bone, since it contains numerous porosities with considerable randomness of orientations, the results were calculated for averaged values for each porosity's orientation and aspect ratio. Figures 9(a)–9(c) show normalized axial Young's modulus versus volume fraction of osteon porosities having

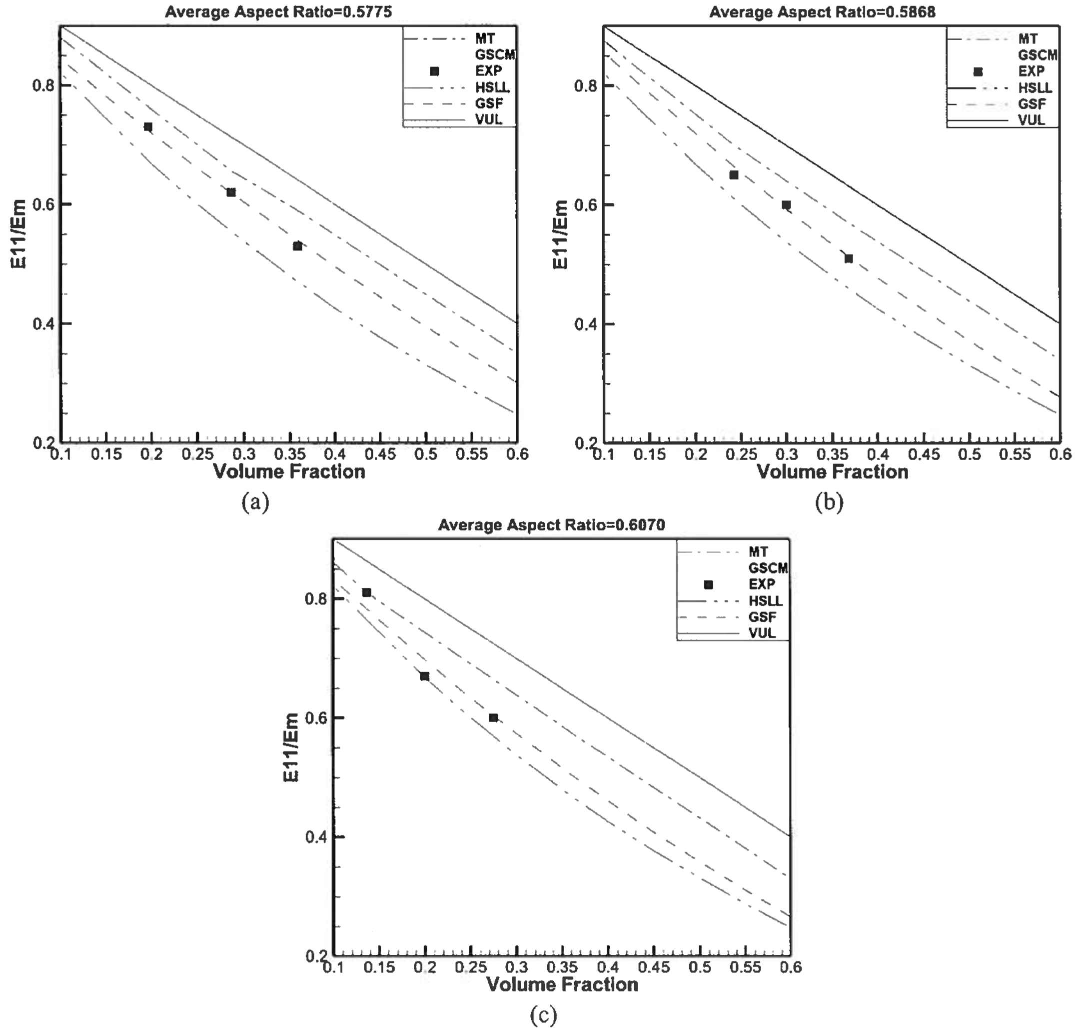

FIG. 9: Normalized axial Young's modulus vs. porosity for the osteons having the same average aspect ratio (a) results at average aspect ratio of 0.5775, (b) results at average aspect ratio of 0.5868, (c) results at average aspect ratio of 0.6070 (MT: Mori–Tanaka, GSCM: generalized self-consistent method, GSF: generalized stiffness formulation, VUL: Voigt upper limit, HSLL: Hashin–Shtrikman lower limit)

the same average aspect ratios: (a) 0.5775, (b) 0.5868, and (c) 0.6070. The figures compare results for the numerical solutions of the MT, GSCM, and GSF. Also plotted for the sake of comparison are bounds according to the Voigt upper limit (VUL) and Hashin–Shtrikman lower limit (HSLL). The plots show that all the normalized stiffness values fall within the upper and lower bounds and also show that osteonal elastic properties are highly dependent on the porosities' volume fractions and shapes. Although all three homogenization methods return close value estimates of stiffness, the GSF results are in closer agreement with measured stiffness values from the indentation tests. This finding is perhaps a testament to the fact that GSF considers the orientation and the positions of the actually segmented numerous microsized inclusions inside the osteons. From Hage and Hamade (2020), comparing values fixed at the same volume fraction and aspect ratio, GSF estimates that a change of average orientation for the pores from 0 to 45° results in a small but distinguishable change in the osteonal normalized modulus of elasticity estimated around 2.57%. As for pores locations, the results for the change in the location was about 2% between a composite's cubical normalized modulus having inclusions positioned at the boundaries of the RVE as compared with another with inclusions clustered at the center of the cube. Taking into consideration the combined effect of location and orientation, GSF estimates that the effect due to these two attributes amounts to a few percentage points. The effect of porosities' orientation and location, albeit being relatively small as compared to the more pronounced effect induced by the volume fraction and aspect ratio attributes, may enhance bone elastic stiffness estimates to approach those measured experimentally.

Figure 10 show plots of normalized axial Young's modulus (E_{11}/E_m) versus average aspect ratio for osteons having the same volume fraction values of (a) 0.1969, (b) 0.287, and (c) 0.368. These values are developed from actual slides such as those segmented in Figs. 3–5. The plots compare solutions numerical solutions calculated using MT, GSCM, and GSF homogenization schemes in addition to the experimental results, EXP. The plots show a decreasing in the elasticity constant as porosities become more rounded (in general agreement with what MT and GSCM predicts). The plots also suggest that the numerical results for the GSF homogenization scheme are in closer congruence with the experimental indentation results than MT and GSCM.

As a summary for Figs. 9 and 10, Table 2 lists the percent difference in values between the normalized axial Young's modulus generated by MT, GSCM, and GSF methods with all being compared to experimental indentation data. The homogenization results utilizing the GSF method at AR of 0.5775, 0.5868, and 0.6070 match well with the experimental results with bounding errors ranging from –6.17 to 4.44%. These GSF estimates that take into account the porosity orientation, location, and size of lacunae are found to provide closer estimates than those provided by either MT (2.47 to 13.33%) or GSCM (–1.23 to 11.11%) over the range of AR and VF considered.

6. CONCLUSIONS

A novel combination of automated image segmentation and numerical homogenization is developed and applied to secondary osteons of cortical bones. The osteon is modeled as a bio-composite matrix embedded by porous inclusions, namely the osteonal microconstituents (lacunae, Haversian canals, and canaliculi) and as a transversely isotropic material. The porosities were examined microscopically. Determined are the effects of the corresponding volume fractions, shapes, orientations, numbers, and locations in the matrix on the elastic longitudinal Young's modulus. Therefore, accounted for are the effects of cortical bone pores' sizes and shapes on osteon composite stiffness.

Using image segmentation based on the authors' recent works (Hage and Hamade, 2013a,b, 2014, 2015, 2016), the porosities (Haversian canals, lacunae, and canaliculi) in demarcated secondary osteons are segregated into separate digital images. Areas, elliptical major–minor axis length, orientations, and the coordinates for each one of the individual pores in the images are identified. The said parameters were used to calculate the inclusions' volume fraction vectors, aspect ratio vectors, orientations, and location in the matrix. These represent the total input vector needed to calculate the Eshelby tensors and, consequently, the normalized axial Young's modulus.

Numerical solutions of osteon stiffness based on actual digitally segmented images, microsized are determined using three different homogenization techniques are obtained. These three methods are: (1) MT, (2) GSCM, and (3) GSF advanced by Hage and Hamade (2020). To corroborate the accuracy of the stiffness results of the three employed homogenization methods, experimental microindentations hardness measurements were conducted on the same image locations in the secondary osteons. The osteonal axial Young's modulus values were determined from

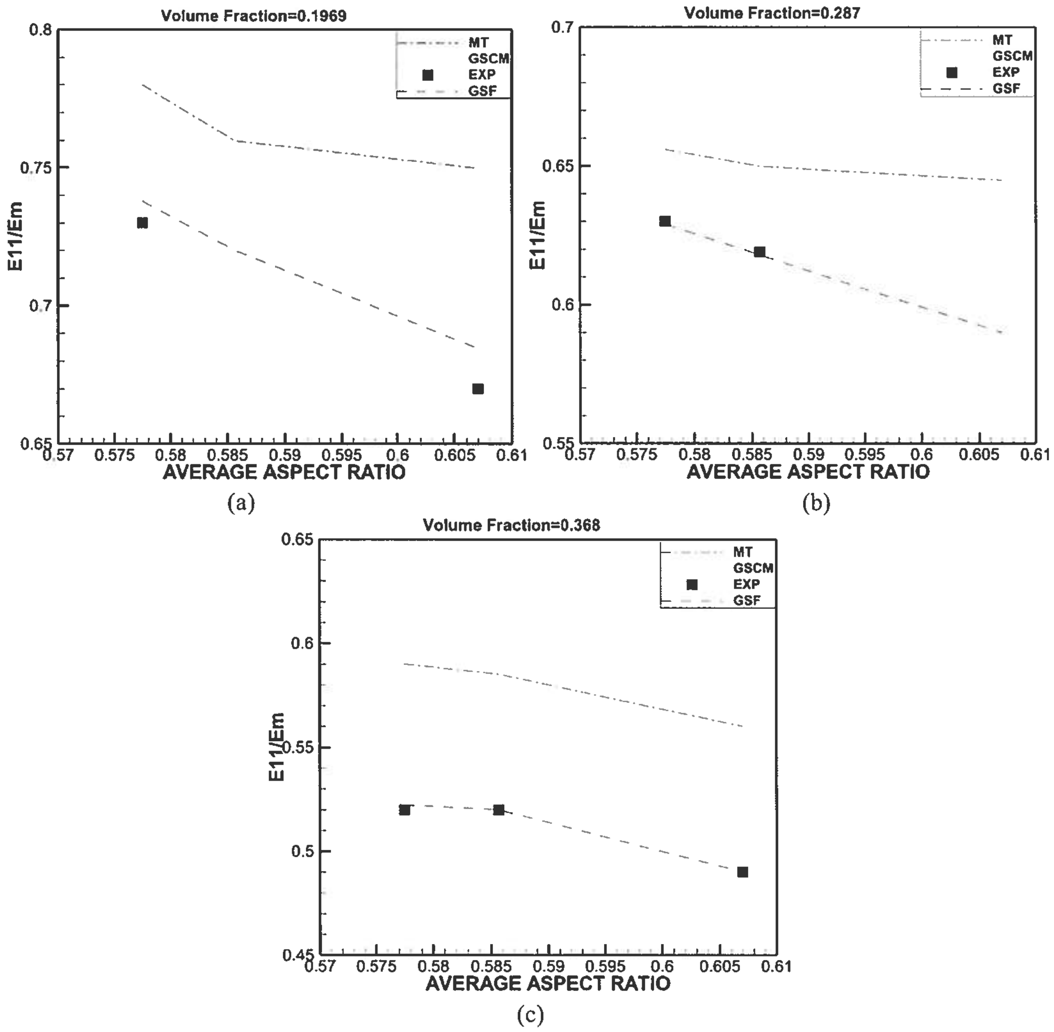

FIG. 10: Normalized axial Young's modulus vs. average aspect ratio for osteons having the same volume fraction values; results at volume fraction of (a) 0.1969, (b) 0.287, (c) 0.368 (MT: Mori–Tanaka, GSCM: Generalized self-consistent method, EXP: experimental results, GSF: numerical results using the developed homogenization code)

TABLE 2: Difference (%) between normalized axial Young's modulus generated by MT, GSCM, and GSF models [all difference (%) values are as compared to experimental measurements]

Osteon average AR = 0.5775				Osteon average AR = 0.5868				Osteon average AR = 0.607			
VF	MT	GSCM	GSF	VF	MT	GSCM	GSF	VF	MT	GSCM	GSF
0.1969	9.5%	9%	2.37%	**0.24**	7.69%	5.38%	3.08%	**0.137**	2.47%	–1.23%	–6.17%
0.287	5.81%	4.84%	–3.23%	**0.32**	5.00%	3.33%	–2.50%	**0.2**	13.33%	11.11%	4.44%
0.368	11.32%	7.55%	1.47%	**0.37**	5.88%	5.49%	1.18%	**0.275**	10.20%	8.16%	–1.02%

force-penetration data generated by the Vickers hardness tests. The numerically calculated osteon stiffness values compared favorably against the experimental stiffness values from the microindentation tests. Though numerical stiffness results from all three methods compare favorably with experimental stiffness values, GSF method exhibits closer agreements. As such, GSF homogenization represents an innovative procedure for estimating osteonal stiffness based on microscopic image analysis. As such, this microstructural bone mechanical modeling based on microstructure scale imaging may aid in the field of orthopedics biomechanics. Examples of such applications may include bone screw design of bone screws (Čada et al., 2017) or strength-related analyses for screws in repairs of femoral neck fractures (Frydrýšek et al., 2018).

ACKNOWLEDGMENTS

This work is made possible by the financial support of the Lebanese National Council for Scientific Research (CNRS) award No. 103087. The authors also wish to acknowledge the support of the University Research Board at the American University of Beirut.

REFERENCES

Barkaoui, A., Chamekh, A., Merzouki, T., Hambli, R., and Mkaddem, A., Multiscale Approach Including Microfibril Scale to Assess Elastic Constants of Cortical Bone Based on Neural Network Computation and Homogenization Method, *Int. J. Numer. Methods Biomed. Eng.*, vol. **30**, no. 3, pp. 318–338, 2014.

Budiansky, B., On the Elastic Moduli of Some Heterogeneous Materials, *J. Mech. Phys. Solids*, vol. **13**, no. 4, pp. 223–227, 1965.

Budyn, É. and Hoc, T., Analysis of Micro Fracture in Human Haversian Cortical Bone under Transverse Tension Using Extended Physical Imaging, *Int. J. Numer. Methods Eng.*, vol. **82**, no. 8, pp. 940–965, 2010.

Čada, R., Frydrýšek, K., Sejda, F., Demel, J., and Pleva, L., Analysis of Locking Self-Taping Bone Screws for Angularly Stable Plates, *J. Med. Bio. Eng.*, vol. **37**, no. 4, pp. 612–625, 2017.

Eshelby, J., Elastic Inclusions and Inhomogeneities, *Prog. Solid Mech.*, vol. **2**, no. 1, pp. 89–140, 1961.

Eshelby, J.D., The Determination of the Elastic Field of an Ellipsoidal Inclusion, and Related Problems, *Proc. R. Soc. London A: Math., Phys. Eng. Sci.*, pp. 376–396, 1957.

Fritsch, A. and Hellmich, C., Universal Microstructural Patterns in Cortical and Trabecular, Extracellular and Extravascular Bone Materials: Micromechanics-Based Prediction of Anisotropic Elasticity, *J. Theor. Biol.*, vol. **244**, no. 4, pp. 597–620, 2007.

Frydrýšek, K., Šír, M., and Pleva, L., Strength Analyses of Screws for Femoral Neck Fractures, *J. Med. Bio. Eng.*, vol. **38**, no. 5, pp. 816–834, 2018.

Hage, I.S. and Hamade, R.F., Segmentation of Histology Slides of Cortical Bone Using Pulse Coupled Neural Networks Optimized by Particle-Swarm Optimization, *Comput. Med. Imaging Graphics*, vol. **37**, pp. 466–474, 2013a.

Hage, I.S. and Hamade, R.F., Structural-Feature-Attribute-Based Segmentation of Optical Images of Bone Slices Using Optimized Pulse Coupled Neural Networks (PCNN), in *ASME 2013 Intl. Mech. Eng. Congr. Exposition*, American Society of Mechanical Engineers, p. V03BT03A019, 2013b.

Hage, I.S. and Hamade, R.F., Toward Quantifying Geometric Microstructural Differences between Primary and Secondary Osteons via Segmentation, in *2nd Middle East Conf. on Biomedical Engineering*, IEEE, pp. 371–374, 2014.

Hage, I.S. and Hamade, R.F., Automatic Detection of Cortical Bones Haversian Osteonal Boundaries, *AIMS Med. Sci.*, vol. **2**, pp. 328–346, 2015.

Hage, I.S. and Hamade, R.F., Geometric-Attributes-Based Segmentation of Cortical Bone Slides Using Optimized Neural Networks, *J. Bone Miner. Metab.*, vol. **34**, pp. 251–265, 2016.

Hage, I.S. and Hamade, R.F., Intracortical Stiffness of Mid-Diaphysis Femur Bovine Bone: Lacunar-Canalicular Based Homogenization Numerical Solutions and Microhardness Measurements, *J. Mater. Sci.: Mater. Med.*, vol. **28**, no. 135, pp. 1–14, 2017.

Hage, I.S. and Hamade, R.F., An Experimentally Validated Combined Stiffness Formulation for a Finite Domain Considering Volume Fraction, Shape, Orientation, and Location of a Single Inclusion, *Int. J. Appl. Mech.*, vol. **10**, no. 1, p. 185001, 2018.

Hage, I.S. and Hamade, R.F., Experimentally Validated Combined Stiffness Expression for Finite Domain Containing Multiple Inclusions, *C.R. Méc.*, vol. **348**, no. 2, pp. 113–135, 2020.

Hage, I.S., Seif, C., Hage, R., and Hamade, R.F., A Verified Non-Linear Regression Model for Elastic Stiffness Estimates of Finite Composite Domains Considering Combined Effects of Volume Fractions, Shapes, Orientations, Locations, and Number of Multiple Inclusions, in *ASME 2018 Intl. Mechanical Engineering Congress and Expo.*, American Society of Mechanical Engineers, p. V009T12A022, 2018.

Hamed, E., Lee, Y., and Jasiuk, I., Multiscale Modeling of Elastic Properties of Cortical Bone, *Acta Mech.*, vol. **213**, no. 1, pp. 131–154, 2010.

Li, S., Wang, G., and Sauer, R.A., The Eshelby Tensors in a Finite Spherical Domain—Part II: Applications to Homogenization, *J. Appl. Mech.*, vol. **74**, pp. 784–797, 2007.

Mori, T. and Tanaka, K., Average Stress in Matrix and Average Elastic Energy of Materials with Misfitting Inclusions, *Acta Metallurg.*, vol. **21**, no. 5, pp. 571–574, 1973.

Mura, T., *Micromechanics of Defects in Solids*, Springer Science and Business Media, 2013.

Neil, D.X. and Guo, X.E., Prediction of Cortical Bone Elastic Constants by a Two-Level Micromechanical Model Using a Generalized Self-Consistent Method, *J. Biomech. Eng.*, vol. **128**, no. 3, pp. 309–316, 2006.

Nikolov, S. and Raabe, D., Hierarchical Modeling of the Elastic Properties of Bone at Submicron Scales: The Role of Extrafibrillar Mineralization, *Biophys. J.*, vol. **94**, no. 11, pp. 4220–4232, 2008.

Novitskaya, E., Hamed, E., Li, J., Jasiuk, I., and McKittrick, J., Correlation of Multi-Scale Modeling and Experimental Results for the Elastic Moduli of Cortical and Trabecular Bone, in *Mech. Biol. Syst. Mater.*, vol. **5**, pp. 99–107, 2013.

Oliver, W.C. and Pharr, G.M., Measurement of Hardness and Elastic Modulus by Instrumented Indentation: Advances in Understanding and Refinements to Methodology, *J. Mater. Res.*, vol. **19**, no. 1, pp. 3–20, 2004.

Oliver, W.C. and Pharr, G.M., Nanoindentation in Materials Research: Past, Present, and Future, *MRS Bulletin*, vol. **35**, no. 11, pp. 897–907, 2010. DOI: 10.1557/mrs2010.717

Parnell, W.J., Vu, M., Grimal, Q., and Naili, S., Analytical Methods to Determine the Effective Mesoscopic and Macroscopic Elastic Properties of Cortical Bone, *Biomech. Model. Mechanobiol.*, vol. **11**, no. 6, pp. 883–901, 2012.

Rho, J., Zioupos, P., Currey, J., and Pharr, G., Variations in the Individual Thick Lamellar Properties within Osteons by Nanoindentation, *Bone*, vol. **25**, no. 3, pp. 295–300, 1999.

Sun, C.T. and Li, S., Three-Dimensional Effective Elastic Constants for Thick Laminates, *J. Composite Mater.*, vol. **22**, no. 7, pp. 629–639, 1988.

Yoon, Y.J. and Cowin, S.C., The Estimated Elastic Constants for a Single Bone Osteonal Lamella, *Biomech. Model. Mechanobiol.*, vol. **7**, no. 1, pp. 1–11, 2008.